Plourde, Frederic, Farida Cheriet, and Jean Dansereau. "Semiautomatic Detection of Scoliotic Rib Borders from Posteroanterior Chest Radiographs." IEEE Transactions on Biomedical Engineering, Vol. 59, No. 4 (2012) pp. 909-919.

doi: http://dx.doi.org/10.1109/TBME.2011.2168394

Semi-Automatic Detection of Scoliotic Rib Borders From Postero-anterior Chest Radiographs

Frédéric Plourde, Farida Cheriet, *Associate Member, IEEE*, Jean Dansereau

Abstract— 3D assessment of scoliotic deformities relies on an accurate 3D reconstruction of bone structures from biplanar X-rays, which requires a precise detection and matching of anatomical structures in both views. In this paper, we propose a novel semi-automated technique for detecting complete scoliotic rib borders from PA-0º and PA-20º chest radiographs, by using an edge-following approach with multiple-path branching and oriented filtering. Edge-following processes are initiated from user starting points along upper and lower rib edges and the final rib border is obtained by finding the most parallel pair among detected edges. The method is based on a perceptual analysis leading to the assumption that no matter how bent a scoliotic rib is, it will always present relatively parallel upper and lower edges. The proposed method was tested on 44 chest radiographs of scoliotic patients and was validated by comparing pixels from all detected rib borders against their reference locations taken from the associated manually delineated rib borders. The overall 2D detection accuracy was 2.64 ± 1.21 pixels. Comparing this accuracy level to reported results in the literature shows that the proposed method is very well suited for precisely detecting borders of scoliotic ribs from PA-0º and PA-20º chest radiographs.

***Index Terms*—Scoliosis, chest radiographs, rib detection, edge following, oriented filtering, perceptual parallelism**

I. INTRODUCTION

Stereoradiography consists in reconstructing 3D anatomical structures using two planar X-ray views taken from different angles. Prior to 3D reconstruction, relevant structures in both planar radiographic views need to be detected and matched. The present paper focuses strictly on this crucial 2D detection step, applied to rib detection in chest radiographs.

Currently, at the Research Center of Sainte-Justine University Hospital Center (UHC) in Montreal, we utilize a completely manual rib detection technique which requires a technician to place eleven markers on every rib midline in two postero-anterior X-ray images, namely, the PA-0º and PA-20º views, which are oriented toward the patient at respectively 0º and 20º from the horizontal. This manual detection step is very time-consuming and currently limits the associated clinical applications. Indeed, a radiology technician takes about two hours to place all the markers in both radiographs [1]. Another limitation is that the current method is only concerned with rib midlines, leading to a wireframe 3D model in which information from actual rib borders is discarded. Finally, the 3D geometry of the ribs is completely operator dependent, which prevents the extraction of clinical indices from the 3D model of the rib cage for 3D assessment of scoliotic deformities. However, scoliosis involves a rib hump mainly due to a 3D axial rotation of the ribs, which is visible on the back of the trunk and is considered as the main concern for the patient. Thus, it is of paramount importance to improve the accuracy of the 3D reconstruction of the rib cage to be able to take into account the rib hump in the clinical assessment of scoliosis. A prerequisite task for an accurate 3D reconstruction is automatic matching of the anatomical structures identified in a pair of views. Thus, the detection of rib borders, instead of rib midlines, will lead to an automatic matching of high level primitives describing each rib as a whole instead of a set of markers manually identified by an operator, hence providing a more accurate 3D reconstruction of the rib cage.

Rib detection from PA chest radiographs has been investigated for the past three decades. However, most of the proposed solutions apply only to the dorsal portions of the ribs and are strictly concerned with PA-0º chest radiographs. Also, some of them are intended for rib subtraction screening applications and are thus limited to detecting ribs located over the lung fields. Furthermore, very few of the methods are concerned with scoliotic ribs. Existing rib detection methods are not suitable for detecting scoliotic ribs for the following reasons. First, because of their large variability in shape and curvature between different patients, scoliotic ribs would not be properly detected using parametric curve fitting techniques [2,3,4,5] or parametric curve-searching algorithms such as the modified Hough transform [3,6]. Also, techniques using global spatial filtering and rib reconnection through rule-based reasoning [2,3,4,5,7] would often miss the edges at rib crossings near the rib cage border, due to high overlapping and locally reduced contrast. In addition, methods based on vertical profile analysis [4,5,8,9] would also encounter major

Manuscript received February 2, 2011.

F. Plourde and F. Cheriet are with the Department of Computer Engineering, Ecole Polytechnique de Montreal, PO Box 6079, Station Centre-Ville, Montreal, QC, Canada, H3C 3A7 (frederic.plourde@polymtl.ca), (farida.cheriet@polymtl.ca).

J. Dansereau is with the Department of Mechanical Engineering, Ecole Polytechnique de Montreal, PO Box 6079, Station Centre-Ville, Montreal, QC, Canada, H3C 3A7 (jean.dansereau@polymtl.ca).

All of the above authors are also with the Sainte-Justine Hospital Research Center, 3175 Cote-Sainte-Catherine, Montreal, QC, Canada, H3T 1C5.

limitations, as they greatly rely on assumptions that the ribs are strictly horizontally-oriented (in their dorsal portions) and that the intercostal space is approximately constant from one rib to another, which is clearly not the case with scoliotic ribs, as observed in [10]. Yet another approach [6] makes use of active contours (snakes) in order to better delineate actual rib borders, but still relies on the Hough transform to initialize the algorithm. More recent approaches use deformable statistical models [11,12,13], but, although promising results have been reported, only the rib midlines are considered in [13] and information from the rib borders is thus lost. Finally, yet newer approaches make use of iterated training sets (ICPC or MTANN) for per-pixel classification [14] or rib suppression [15]. Although these methods seem suitable for detecting scoliotic rib borders, [14] is strictly interested in detecting dorsal portions of the ribs whereas [15] produces bone-image-like output images, lacking a way to discriminate the ribs from each other.

Our goal is to develop a semi-automatic rib detection method that can accurately delineate the scoliotic rib borders for both the ventral and dorsal rib portions, in either PA-0º or PA-20º angled-down chest radiographs. We previously published a proof of concept of our method in [16] for which we will hereafter give more detailed materials and methods and present an extensive validation. Also, it is to be noted that a team from the Wright State University already implemented and successfully applied our method for rib segmentation in order to obtain 3D reconstructions of the rib cage [17].

II. MATERIALS AND METHODS

A. Overview

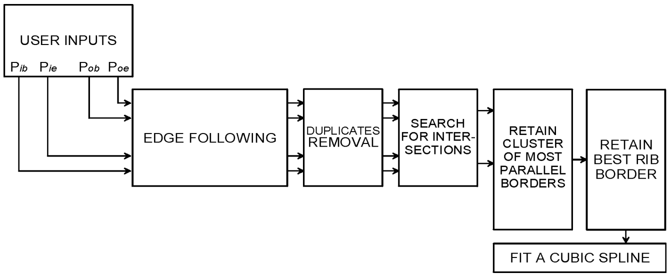

Fig. 1. Block diagram of the proposed method.

In order to meet our goals, we propose herein a novel, semi-automated technique for detecting both dorsal and ventral portions of scoliotic rib borders using an oriented filtering and edge-following approach with multiple-path branching. The key idea behind the proposed method is that, even in cases of great scoliotic deformity, a single rib will always present relatively parallel upper and lower edges. Our method consists in following multiple promising edges simultaneously. For every rib, four edge-following detections are initiated from four user-provided starting points placed along the upper and lower rib edges and the final rib border is obtained by finding the most parallel pair among the detected edges. The block diagram in Fig. 1 shows the different logical units within the proposed solution. Each of them will be analyzed in detail in the following subsections.

B. Radiographic materials and data acquisition system

50 digital chest radiographs of scoliotic patients were randomly selected from the Sainte-Justine UHC radiographic database. All radiographs were produced with a Fuji FCR 7501S device equipped with a Shimadzu UD150L camera. The digitalized images of size 880 X 2140 pixels are eight bits per pixel and compressed in TIFF format. Our method was tested on 44 of these; the other 6 were previously used to build the peak classification statistical model described in section II-D-4. Among those 44 radiographs were 32 PA-0º views and 12 PA-20º views. Each radiograph was manually classified as being of “good quality”, “regular quality” or “poor quality” by a radiology technician. This resulted in a classification of 17 good, 18 regular and 9 poor images. Quality levels were ascertained by taking into account the presence or absence of several undesirable radiographic characteristics such as noise, non-uniform illumination, extra-scoliotic pathologies such as tumors, and radiographic artifacts.

C. User interaction

Scoliotic ribs present very few shape priors due to their irregularities from one patient to another. In that context, semi-automation involving human interaction in both an initialization step and a post-processing step was considered a better approach than full automation. In the following, radiographic ribs consist of an inner edge (*I*), closer to the spine, and an outer edge (*O*), further from it, as shown in Fig. 2. Ribs are assumed to begin (*B*) at the dorsal extremity and end (*E*) at the sternal extremity. Prior to detection, only four user starting points are needed (p_{ib}, p_{ob}, p_{ie}, p_{oe}) for each rib. Their associated starting angles (θ_B and θ_E) are automatically set perpendicular to the lines joining p_{ib} to p_{ob} and p_{ie} to p_{oe}. Thus, the user must be careful that the four starting points be approximately perpendicular to the rib’s orientation at extremities *B* and *E*. No automatic, gradient-driven fine-tuning of the starting points’ locations has been implemented yet. Finally, after detection, the user can manually adjust any rib edge in a corrective post-processing step. This, however, is beyond the scope of this paper and this manual correction step will not be treated further.

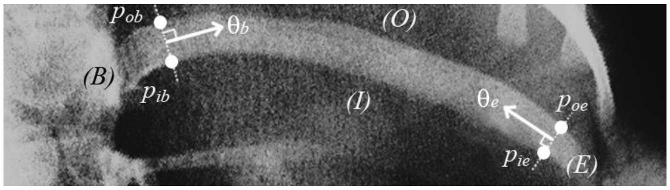

Fig. 2. An illustration of the required four user inputs per rib (p_{ib}, p_{ob}, p_{ie}, p_{oe}). A close-up of the 11th left rib is seen here. θ_b and θ_e are automatically computed perpendicularly to lines joining p_{ob} to p_{ib} and p_{oe} to p_{ie}, respectively. Letters *B, E, I* and *O* indicate the rib’s beginning, end, inner side and outer side, respectively.

D. Multiple-path edge-following

The whole idea behind the proposed rib detection algorithm is to follow a rib's edge, starting from its two extremities (*B* and *E*) and going inwards as if walking along the rib's border, and expecting that these concurrent detections will intersect each other at some edge point in between *B* and *E*. This task is carried out using the edge following paradigm.

Most conventional edge-following methods deal exclusively with binary edges, namely, black or white pixels obtained after filtering and thresholding. However, given a chest radiograph containing variable edge magnitudes and much overlapping between different structures, a global thresholding approach with isotropic filtering would result in the loss of many partial features, resulting in a spurious binary image and diminished edge-following capabilities [18]. We propose a modified edge-following approach, applied directly to grayscale images with no thresholding, using only oriented filtering and multiple-path branching. A block diagram of the technique is presented in Fig. 3.

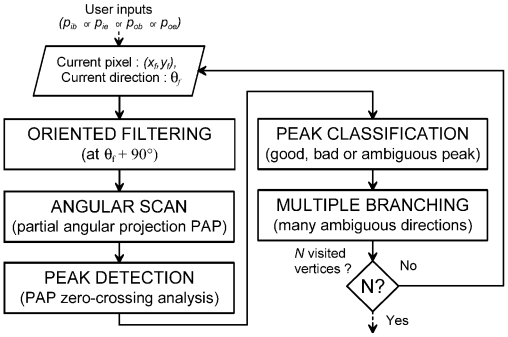

Fig. 3. The proposed multiple-path edge-following method.

1) Oriented filtering

Radiographic ribs present a great deal of mutual crossings as well as overlappings with other structures at various angles. This poses serious difficulties to edge following algorithms, which are likely to fail at detecting a complete rib by mistakenly following a border that does not belong to it but to another structure such as a clavicle. Most conventional edge-following methods compute edge-followed angles in either an 8-neighbor square-grid or a 6-neighbor hexagonal-grid discrete space. However, these choices limit the angular resolution to 45 or 60-degree steps, respectively. Since crossings between different structures may arise at any angle in a real radiograph, better results can be obtained using a continuous addressing space, as explained in [19]. Bilinear interpolation was used to access gray values in between pixels. The proposed oriented filtering approach uses the anisotropic filter depicted in Fig. 4.

Assuming that a grayscale radiographic image can be seen as a discrete function $f(x,y)\in[0,1...255]$ *with* $x,y\in[0,1...K-1]$, the filtered image *g(x,y)*, using the convolution mask *h(s,t)*, can be expressed by a 2-D discrete convolution [20] as in:

$$g(x,y)=\sum_{s=-K/2}^{K/2}\sum_{j=-K/2}^{K/2}f(x+s,y+t)h(s,t)\,. \tag{1}$$

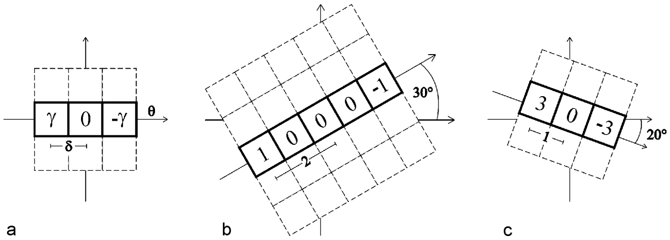

Fig. 4. Anisotropic filter h(s) used in oriented filtering step. (a) Unrotated 1D version. The filter output gives approximations of image partial first-order derivatives of magnitude γ, scale δ and orientation θ. Two rotated instances of the filter are shown in (b) with γ = 1, δ = 2, θ = 30º and (c) with γ = 3, δ = 1 and θ = -20°.

This expression only applies to the unrotated version of the proposed filter depicted in Fig. 4. For its correct implementation at any given orientation, the steerable filter paradigm [21] can be used, but by taking advantage of the fact that the filter *h(s)* is indeed 1-D and contains only 2 non-negative values, (1) can be rewritten as:

$$g^{\theta}(x,y)=\begin{bmatrix}\gamma & -\gamma\end{bmatrix}\begin{bmatrix}f(x-\delta\sin\theta,y-\delta\cos\theta)\\ f(x+\delta\sin\theta,y+\delta\cos\theta)\end{bmatrix}+\mu\,, \tag{2}$$

which is the difference between the image translated by δ at angle θ and the same image translated by δ in the opposite direction (at θ + 180º). Contrast is controlled by γ, δ is the depth of the filtering operation and the mean grayscale level is set by μ. Popular image-editing software packages implement (2) under the name "Emboss filter". In fact, when the output is centered around grayscale level 128 (μ=128), *g(x,y)* looks like an embossed image, featuring hills and valleys, as in Fig. 5. However, in our method, μ = 0. The parameter γ was empirically set to 3 because this led to a good tradeoff between contrast and border thickness.

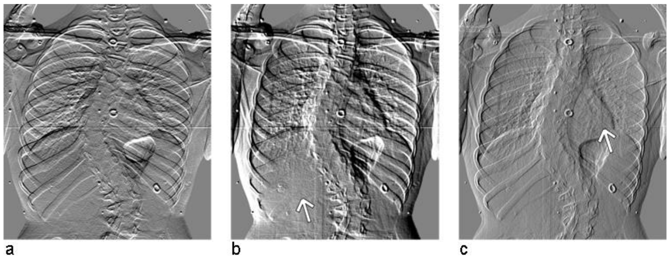

Fig. 5. Embossed image from the anisotropic filter in (2) applied to a chest radiograph of a scoliotic patient with centered grayscale (μ=128). Orientation θ, contrast γ and depth δ are all controllable parameters. Shown here are (a) θ = 90º, γ = 5, δ = 3; (b) θ = 40º, γ = 6, δ = 5; (c) θ = 336º, γ = 1, δ = 2. The white arrows point out zones where ribs have almost completely disappeared.

By noticing the disappearance of ribs 9R to 12R in Fig. 5b and ribs 3L to 8L in Fig. 5c, it becomes obvious that it is possible to "clean" crossing edges by using the proposed anisotropic filter properly aligned with respect to overlapping structures. In fact, this consists, at each step of the edge-following process, in applying the anisotropic filter perpendicularly to the current edge-followed rib orientation. It has been observed that doing so emphasizes the currently followed border while attenuating most of the undesirable edges (see Fig. 6). The notation $g^{\perp}(x,y)$ will be used when referring to the perpendicularly filtered image.

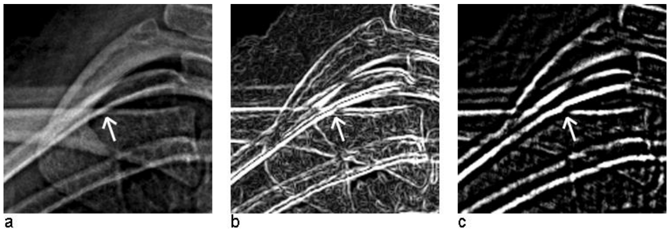

Fig. 6. Rib crossing attenuation. (a) Source image showing rib 3R. The white arrow indicates an ambiguous crossing between the rib and the right clavicle. (b) Regular Sobel filtering emphasizes all edges regardless of their orientation. (c) The anisotropic filter in (2) is applied perpendicularly to the third rib's orientation at the crossing point.

2) *Angular search*

Even after applying the oriented filtering, some remaining concurrent edges can still mislead the edge following process, especially when these are strong edges almost parallel to the followed rib border. Throughout this paper, we will use the term "ambiguous" to refer to any location along the followed border at which two or more significant edges cross each other. Contrary to conventional edge-following algorithms, the proposed method has the ability to follow multiple promising paths simultaneously, thus reducing the likeliness of being misled in the presence of ambiguous edge crossings. The underlying idea is to see image pixels as potential vertices v in an n-ary rooted tree T [22]. The notion of seeing edge-following as a graph-searching process is not new [23]. For each visited vertex v_i^j, there is a variable number n of followed children with a maximum of N vertices in T. In this notation, v_i^j represents the i^{th} visited vertex at depth j and v_1^0 is the root vertex input by the user. Typical detection results, as shown in Fig. 7, will thus appear as a tree-like set of visited pixels belonging to many different detected borders, among which the actual rib edge is expected to be found.

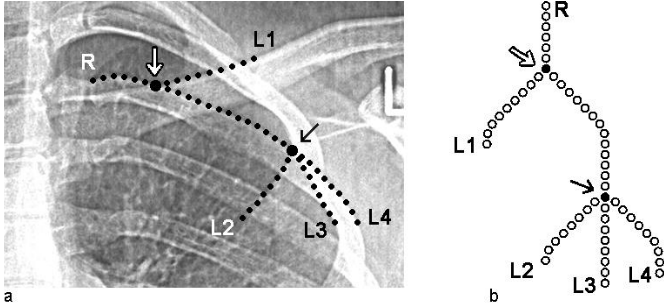

Fig. 7. Multiple-path branching, in which visited image pixels become vertices in a tree graph. (a) A close-up of a chest radiograph showing progress of the multiple-path edge-following after 55 visited pixels. (b) The associated tree graph T. The white arrow shows the first ambiguous pixel encountered whereas the black arrow shows the second one. Letters point out special vertices. "R" stands for "Root" and "L" for "leaf".

From a specific parent vertex v_i^j in the edge-following process, children are always chosen λ pixels away. This distance is called the edge-following "step" and was empirically fixed at $\lambda = 5$. At each step, child vertices v_i^{j+1} are obtained by computing the partial angular projection presented in (3) below and by detecting and localizing its local maxima. Each local maximum is associated with an edge orientation and represents a potential child vertex, as shown in Fig. 8. The partial angular projection (PAP) can be expressed as:

$$\rho(\theta)=\sum_{r=0}^{R} g^{\perp}(r\cos\theta - x_f, r\sin\theta - y_f) \qquad \text{with } \theta=[\theta_f-\tau,\theta_f+\tau]. \tag{3}$$

$g^{\perp}$ is expressed in polar coordinates (r, θ), centered at the current vertex location (x_f, y_f) and $\rho(\theta)$ is the PAP of $g^{\perp}$ on the θ axis, limited to $\theta \in [\theta_f-\tau,\theta_f+\tau]$ and $r \in [0,R]$. Fig. 8 summarizes all the steps seen thus far, from the oriented filtering to the PAP computation.

3) *Peak detection*

Local maxima in $\rho(\theta)$ are simply detected by analyzing zero-crossing occurrences in the PAP derivative $\rho'(\theta)$, computed with simple finite differences as shown in Fig. 8e.

Care is to be taken in choosing τ and R. If τ is chosen too small, the field of vision in front of the followed direction will be too narrow and concurrent edges away from θ_f are likely to be missed. On the other hand, if τ is set too large, then projection values become irrelevant near $\theta_f \pm 90^o$ because of prior perpendicular filtering. Likewise, if R is too small, the PAP will show nothing but noisy patterns, while setting R too large will flatten out the PAP to a constant value approaching μR. It was observed that $\tau = 35°$ and $R = 30$ led to good results for a wide range of radiographs.

4) *Peak classification*

At this stage, significant local maxima contained in $\rho(\theta)$ have all been detected and localized. From now on, these will be referred to as "peaks". For each peak p_i located in a given PAP, $\theta_{P,i}$, $\theta_{L,i}$ and $\theta_{R,i}$, namely, the peak summit angle, the left limit angle and the right limit angle of peak p_i, have been computed (see Fig. 8e). Two more quantities need to be computed for each p_i. These are the peak relative area Λ_i (4) and the peak angular shift ε_i, (5) expressed as:

$$\Lambda_i=\frac{\left(\sum_{\theta=\theta_{R,i}}^{\theta_{L,i}}\rho(\theta)\right)-\min\left(\rho(\theta)\right)\cdot\left|\theta_{L,i}-\theta_{R,i}\right|}{\sum_{j=1}^{n}\Lambda(p_j)} \tag{4}$$

$$\varepsilon_i=\left|\theta_{P,i}-\theta_f\right| \tag{5}$$

For a given PAP, every peak p_i provides potential child vertices that may be followed in the next edge-following step. If more than one peak is detected, it is hazardous to simply follow the strongest peak (i.e. having the largest area *Λi*), as it may belong to an ambiguous edge from any overlapping structure. Neither is it efficient to follow all the peaks at every step for obvious reasons of memory usage and computational load. In fact, if n is chosen too large at every step, the associated detection tree will be too broad and the maximum number N of total vertices will be reached before getting to the end of the rib edge of interest. On the other hand, if n is chosen too small at every step, the detection tree will be too narrow and only a few edges will be explored thoroughly, thus incurring the risk of missing the rib edge of interest.

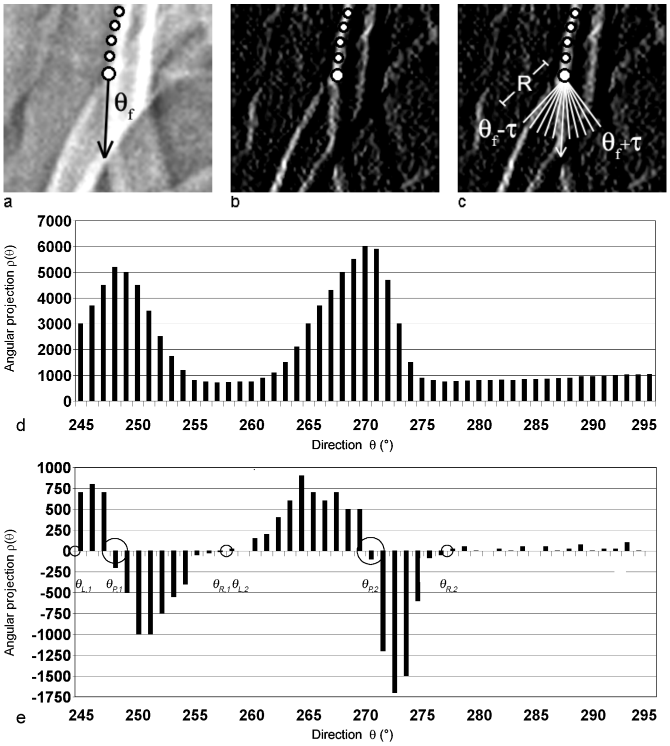

Fig. 8. Oriented filtering and partial angular projection (PAP). (a) Edge-following has already progressed and is now located at an ambiguous pixel (larger white dot) with current edge-followed orientation θ_f. (b) $g^{\perp}$, the filtered image using (2) with $\theta = \theta_f + 90°$, $\delta = 2$ and $\gamma = 6$. (c) Angular scan at work. R pixels are summed along each line oriented from $\theta_f - \tau$ to $\theta_f + \tau$ in $g^{\perp}$. Scan lines are separated by one-degree angles. (d) Plot of the associated partial angular projection (PAP). (e) Local maxima detection in PAP. The first derivative of the PAP in (d) is computed here using finite differences and directions $\theta_{L,1}$,$\theta_{R,1}$,$\theta_{P,1}$ and $\theta_{L,2}$,$\theta_{R,2}$,$\theta_{P,2}$ are found (circled).

Therefore, what is needed is a measure of the ambiguity at any specific pixel along the way. Such a measure will allow us to adaptively set n, choosing fewer or more child vertices to follow at each step, thus maximizing the chances of correctly detecting the edge of interest before reaching N visited vertices. Here, we developed a classification model to predict which peaks to follow depending on selected characteristics.

Potential peaks p_i were modeled as two-value attribute vectors *(x1, x2)*. The chosen peaks' attributes are the ones presented in (5), that is:

$$\mathbf{x}_i = (\Lambda_i, \varepsilon_i). \qquad (6)$$

To train the classifier, 18 radiographic ribs were selected from 6 different chest radiographs. Of those 18 ribs, 6 were free of any significant ambiguous edge crossings, 6 crossed significant edges fewer than five times from beginning until end, and 6 had more than five significant edge crossings along the way. Our edge-following algorithm was run on both the inner and outer edges of all 18 chosen rib borders, except that at each step of the edge-following process, the next followed orientation θ_f was manually selected by a user, clicking the correct peak inside the PAP displayed on screen. All the selected peaks were given class ω_1 (*i.e.* "good" peaks) whereas all the rejected peaks were given class ω_2 (*i.e.* "bad" peaks). Moreover, in cases of ambiguity, the user could click a "skip" button in order to exclude all peaks in the current PAP. In that manner, only non-ambiguous, well-defined edges were sampled within the training set. Fig. 9 shows the distribution of the sampled peaks in attribute space. Each dot represents a peak p_i located at $(\Lambda_i, \varepsilon_i)$ within the two-variable attribute space. The horizontal axis represents the relative area from 0 to 1, whereas the vertical axis represents the absolute angular shift in degrees about the center of the PAP.

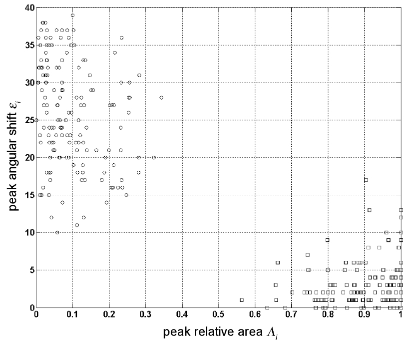

Fig. 9. Scattergram of peaks distribution. Class ω_1 (good peaks) is represented by squares (lower right) and class ω_2 (bad peaks) is represented by circles (upper left).

Looking at Fig. 9, it can be seen that good peaks (class ω_1, bottom right) are generally centered in their PAPs and have large relative areas, whereas bad peaks (class ω_2, top left) are offset from θ_f by 35° on average and have smaller areas. The Parzen windows classification method [23] was used to obtain a non-parametric model of peak density $p_n(\mathbf{x})$ for classes ω_1 and ω_2, as shown in Fig. 10a. This density can be seen as a measure of the probability, for a peak $\mathbf{x}$, to belong to class ω_1 or ω_2. However, this does not tell us anything about peak ambiguity. For that, let us assume that an ambiguous peak is one for which it is not certain whether it is good or bad. Thus, any peak $\mathbf{x}$ falling to low density levels in both classes can be considered ambiguous. To implement this aspect of our model, an extra class ω_3 (ambiguous peaks) was created by setting a low density threshold at $p_n = \xi$, as shown in Fig. 10b. In this manner, one obtains a classification map of ω_1, ω_2 or ω_3 labels for any peak $\mathbf{x} = (\Lambda_i, \varepsilon_i)$ (see Fig. 10b). The choice of ξ directly relates to n, the number of followed child vertices at each edge-following step. Experimentally, it was observed that $\xi = 0.15$ led to good results.

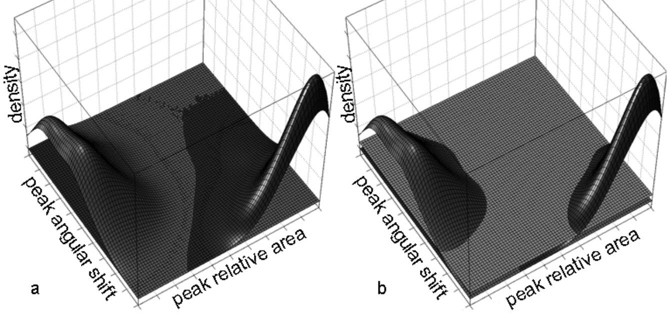

Fig. 10. Peak classification model using Parzen windows. In both graphs, the left hump is class ω_2 (bad peaks) and the right hump is class ω_1 (good peaks). (a) Model with only classes ω_1 and ω_2. (b) Same model with the additional class ω_3 (ambiguous peaks) created by adding a horizontal plane at the low probability threshold of $\xi = 0.15$.

5) *Multiple branching*

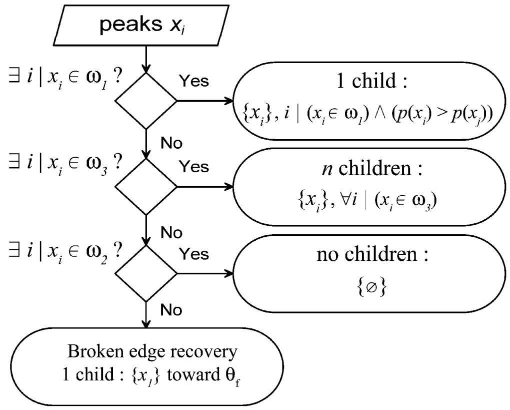

Fig. 11. Decision rules for selection of children after peak classification.

The last element we need in our multiple-path branching is a set of decision rules linking peak selection to probability $p_n(\mathbf{x})$. Fig. 11 depicts the decision rules strategy that was chosen. The idea behind it was to translate the statistical ambiguity brought by our model into a machine-friendly set of rules based on easily calculated probabilities. If there is no ambiguous peak in a given PAP, then we follow the strongest 'good' peak. However, if there is no 'good' peak, then we perform multiple-path branching by following every 'ambiguous' peaks in parallel. Many different strategies were tested but this one was empirically retained because it led to the best results. Also, it can be seen that a 'broken edge recovery' step occurs when the current PAP does not contain any significant peaks. In other words, a recovery strategy is used when the followed edge is lost and consists of reconnecting the edge λ pixels away in the currently followed direction since rib curves are assumed to be smooth.

E. *Perceptual parallelism*

Once all four detection trees T_{ib}, T_{ob}, T_{ie} and T_{oe} have been obtained from their associated starting points and duplicate paths have been removed, all distinct root-to-leaf paths P in those four trees are extracted. A root-to-leaf (RTL) path P is a set of M detected vertices (x_k, y_k), starting at the root vertex and ending at any leaf vertex, and has the following form:

$$P = \{(x_k, y_k)\}, \quad k \in [1, M]. \tag{7}$$

Thus, $P_{T_{ib}}$, $P_{T_{ie}}$, $P_{T_{ob}}$ and $P_{T_{oe}}$ are now defined as the four sets of all RTL paths P extracted from detection trees T_{ib}, T_{ie}, T_{ob} and T_{oe}, respectively. We refer to a specific RTL path within any of these four sets by an index (m or n interchangeably). For example, $P_{n,T_{ib}}$ refers to the nth RTL path in tree T_{ib} wheras $P_{m,T_{oe}}$ refers to the mth RTL path in tree T_{oe}. Now, the problem of detecting the final rib border is equivalent to finding the most parallel pair of paths between the detected paths for the rib's inner edge and those for its outer edge.

But before finding the most parallel pair of paths, complete paths must be obtained, *i.e.* complete inner rib edges or outer rib edges going from rib beginning (B) to rib end (E). These complete paths will thus begin at some tree root vertex and finish at the opposite tree root vertex. Therefore, they will be called root-to-root (RTR) paths. For an RTR path to be identified, there must exist an intersection point I between $P_1 = P_{m,T_{ib}}$ and $P_2 = P_{n,T_{ie}}$, (or equivalently between $P_1 = P_{m,T_{ob}}$ and $P_2 = P_{n,T_{oe}}$), as in:

$$\exists\, I = (i, j) \mid \sqrt{(x_{i,1} - x_{j,2})^2 + (y_{i,1} - y_{j,2})^2} \le \lambda/2. \tag{8}$$

where $(x_{k,1}, y_{k,1}) \in P_1$ and $(x_{k,2}, y_{k,2}) \in P_2$, for any k. Recall that λ is the edge-following step parameter. A complete RTR path Q, of the same form as (7), contains K detected pixels or vertices (x_k, y_k) and is expressed in the following manner:

$$Q = P_{1\{k=1\ldots i\}} \cup P_{2\{k=j\ldots M\}} \mid I = (i, j), \tag{9}$$

with P_1, P_2 being any two inner intersecting RTL paths from $P_{T_{ib}}$ and $P_{T_{ie}}$ respectively, or any two outer intersecting RTL paths from $P_{T_{ob}}$ and $P_{T_{oe}}$ respectively. Then, Q_I and Q_O are the two sets of all intersecting paths between $P_{T_{ib}}$ and $P_{T_{ie}}$, and between $P_{T_{ob}}$ and $P_{T_{oe}}$, respectively.

All that remains to do is to evaluate the perceptual parallelism for each pair of RTR paths taken from Q_I and Q_O. Now let again Q_u be any specific RTR path taken from Q_I and Q_v any RTR path from Q_O, with Q_u being shorter or equal in length than Q_v. Then the rib width function Γ for pair Q_u Q_v, is defined as:

$$\Gamma(k) = \min_{l} \left\{ \sqrt{(x_{k,1} - x_{l,2})^2 + (y_{k,1} - y_{l,2})^2} \right\} \forall l \in Q_v, \tag{10}$$

where $x_{k,1}$ is the x coordinate of the k^{th} point in Q_v, and similarly for $x_{l,2}$, $y_{k,1}$ and $y_{l,2}$. The width function support is $k \in [1, K]$. Fig. 14 depicts $\Gamma(k)$ for two specific RTR paths Q_u and Q_v.

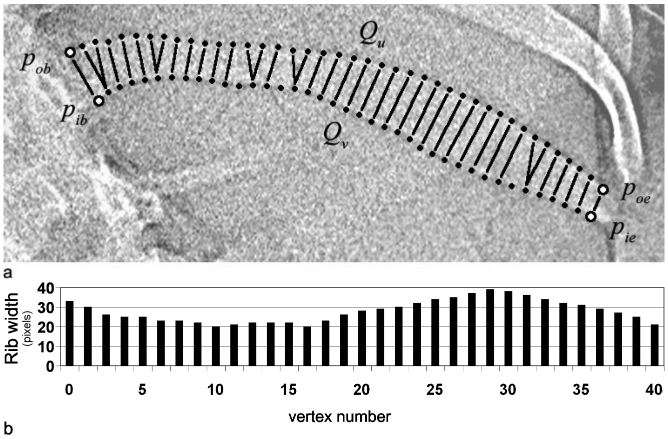

Fig. 14. Simple width function. a) Radiographic rib on which lines show the computed distances to form the rib width function. b) The associated rib width function $\Gamma(k)$.

With the width functions computed for every possible pair Q_I Q_O, it is then possible to compute every pair's perceptual parallelism criterion (PPC) in order to find the final rib border solution. Interesting methods for detecting perceptually parallel curves are detailed in [24,25,26], but when tested in our application, these proved to be too slow. Thus, a somewhat simpler parallel curves detection algorithm had to be developed to ensure acceptable computing times. The key idea behind our method is to realize that truly perceptually parallel edges should produce a totally flat width function, *i.e.* $\Gamma(k) = w$, with w being the rib width. So what is needed is a measure that tells us how close a given width function is to a constant value. We chose to use a least-squares linear fitting between the rib width values and a horizontal line at w to carry out this task. Unfortunately, w is unknown. Contrary to conventional rib detection methods, we strived to stay as general as possible and avoided making morphological assumptions such as fixing the rib width. Hence, w is assumed to be variable and different for all the ribs, which implies that the current rib's width must be estimated. Using the rib width function $\Gamma(k)$ alone, a few choices for setting w are made available by descriptive statistics. The mode Mo of $\Gamma(k)$ was chosen to approximate w because of its stability in the presence of outliers. The proposed perceptual parallelism criterion σ can then be defined as:

$$\sigma = \frac{1}{\sum_{k=1}^{N} \left(\Gamma(k) - \mathrm{Mo}\right)^2}. \tag{11}$$

Using (11), one could find the single most parallel pair of paths and simply use it as the final rib border solution. But that is not quite sufficient. Indeed, it is recalled here that our rib width function $\Gamma(k)$, defined in (10), was deliberately chosen to be very simple for computational reasons. It is an approximation of the real rib width. Moreover, the PPC proposed in (11) lacks robustness in cases of ribs having variable width from beginning to end. Hence, this limits the ability of the algorithm to tell truly parallel paths from other parallel paths.

To get around this problem, we do not simply keep the most parallel pair of paths, but instead, we keep a cluster of the most parallel pairs of paths, expecting that the true solution is contained in that cluster of solutions. The K-means algorithm is used on the σ parameter (PPC) to select this cluster. Finally, the final rib border is selected as being the single smoothest pair of paths in the cluster. The smoothness is computed using the internal energy E_{int} defined in [26]; the chosen pair of paths is thus the one with the least internal energy. The final rib border solution is then obtained by fitting a natural cubic spline with a centripetal model [27] through all of its detected pixels for each of its borders.

F. *Validation of the method*

Using an image editing software package, a technician in radiology was asked to manually delineate each rib's border in all 44 radiographs in our test set. Using a technique very similar to the width function computation in (10), a script was then devised to obtain the perpendicular vector at every detected rib pixel and automatically compute the error (signed distance in pixels) for each detected pixel compared to its reference rib border pixel taken from the validation image. More specifically, for any single detected edge pixel, its reference pixel is the one from the corresponding rib border in the validation image that is closest to a line drawn perpendicularly to a segment joining the current and previous detected pixels.

It is important here to emphasize the fact that our reference rib borders were traced by hand in a discrete space. Thus, the reference's accuracy is comparable to that which our method is capable of attaining. The expression "detection error", as used in the discussion section, is therefore not meant to refer to an error made compared to a gold standard, but rather to the distance (in pixels) between detected and reference pixels. This error can be positive or negative. Furthermore, when referring to the unsigned distance in pixels between the detected and reference rib edge points, the term "absolute distance" will be used to avoid confusion.

The proposed rib detection method was run on all 44 radiographs in the test set, for every rib that had previously provided starting points. The method was implemented in plain non-optimized Matlab language and run on Intel Pentium D 3.40GHz machines with 1GB of RAM. A total of 994 scoliotic ribs were processed. Validation was carried out by running the validation script on the detected ribs and, as shown in Table I, a total of 778,320 pixels were compared against their reference locations (846 pixels per rib, ranging from 102 to 1,479, depending on rib length).

To address the issue of inter-technician variability, we have conducted an additional detection experiment with 3 new users on a reduced test set. 15 radiographs (5 good, 5 regular and 5 poor quality images) were randomly picked from the original set of 44 and were given to each of the 3 users. As in the original study, these users were asked to input 4 starting points per rib on all 24 ribs in their 15-radiograph set. These users were not radiology technicians, but were briefed on how to perform the manual selections. Detection results and inter-technician variability will be presented and discussed below.

III. RESULTS AND DISCUSSION

TABLE I
DETECTION RESULTS

Number of ribs	382 good 408 regular 204 poor
Number of detected ribs	361 good 378 regular 181 poor
Overall rib detection ratio (%)	93
Number of detected pixels for complete dataset	778,320
Average absolute error for complete dataset (pixels)	2.64
Number of divergent ribs	45
Ratio of manually removed pixels (%)	2.1
Corrected number of detected pixels for reduced dataset	761,950
Mean detection error for reduced dataset (pixels)	**$\mu = 0.0026$** **$\sigma = 1.21$**
Average absolute error for reduced dataset (pixels)	**1.24**
Average time to input 96 starting points per radiograph (s)	348

Out of all 994 scoliotic ribs that were processed, the proposed algorithm found border solutions for 920 of them, which corresponds to an average detection ratio of 93%. For the remaining 74 ribs, the edge-following algorithm could not find any solution. Table I summarizes the detection results. Two visual detection results, namely for good and poor quality radiographs, are presented in Fig. 15a,b (see zoomed areas in Fig. 15d,e). Detected borders are delineated in pure white. For the complete set of visual results, the reader is invited to visit the following web page:
http://www.polymtl.ca/liv4d/doc/fred_plourde/index.html.
Fig. 15c shows one particular “missed rib” case, where no intersection occurred between paths p_{ob} and p_{oe}. Path p_{ob} chose to follow the clavicle because of its greater contrast in comparison to the locally faint rib edge (see zoomed area in Fig. 15f). Path p_{oe} diverged from the current rib edge because of a calibration artefact appearing on film as a white dot.

The average absolute error of 2.64 pixels shown in Table I takes into account every single validated pixel from the 994 detected ribs. However, by inspecting the visual results, we noticed that some detected rib border results were very erratic and could get as far as 80 pixels away from their reference rib borders. In fact, by plotting the histogram of detection errors *vs* location along every single rib, it appears obvious that those errors occurred when the edge-following algorithm somehow lost track of the followed rib border. Those samples do not provide us with information about rib detection accuracy itself, but rather give us insight on the probability for the algorithm to lose track of the rib border. Thus, in order to strictly address results concerning the rib border detection accuracy, we excluded from the initial data every rib portion that significantly diverged from its followed rib border. As shown in Table I, we removed the divergent portions from 45 detected ribs, which represented a reduction of 16,370 detected pixels (2.1% of all detected pixels from the complete dataset). The expression “reduced dataset” will be used hereafter to refer to this reduced number of detected pixels, whereas the expression “complete dataset” will be used to refer to all samples from the initial data. Fig. 16 shows the distribution of detection errors for the reduced dataset as well as a Gaussian fit applied to it, for which a general Gaussian model was used with the non-linear least squares method and the least absolute residual (LAR) scheme. This model fitted very well (r^2 = 0.9912 and $RMSE$ = 0.006115) and the overall detection error turned out to be 0.0026 ± 1.21 pixels. The pixels’ actual size is 0.33 mm.

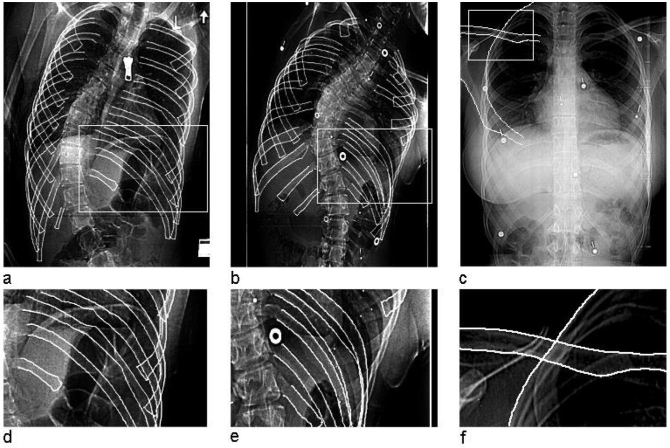

Fig. 15. Visual detection results delineated in pure white. (a,b) Two chest radiographs of scoliotic patients classified as ‘good’ and ‘poor’. c) Missed rib case for rib L4. (d,e) Zooms on details of figures 15a and 15b respectively. f) Zoom on details of figure 15c. White rectangles are zoomed areas.

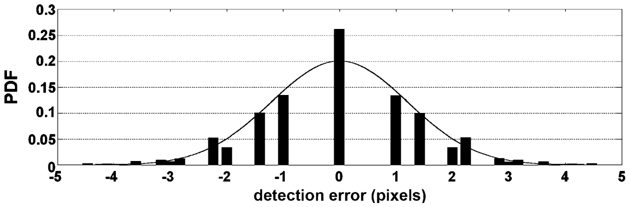

Fig. 16. Distribution of detection errors for the reduced dataset with Gaussian fit (r^2 = 0.9912 and $RMSE$ = 0.006115). Distribution parameters are: μ = 0.0026 pixels and σ = 1.21 pixels.

For comparison purposes, it is also convenient to present the results as absolute distances to reference pixels, as most of the previous methods in the literature do. As shown in Table I, the average absolute distance to reference pixels for the reduced dataset was 1.24 pixels. Analogous results were also obtained separately for good, regular and poor image qualities, and respective detection errors of 0.0024 ± 1.12 pixels, 0.0015 ± 1.16 pixels, 0.0019 ± 1.22 pixels were obtained using the same abovementioned Gaussian model.

Fig. 17 shows the average absolute distance obtained for each rib level, for the three image quality level subsets. The horizontal axis represents the average absolute distance whereas the vertical axis represents the different rib levels, with labels indicating both the number and side of each rib.

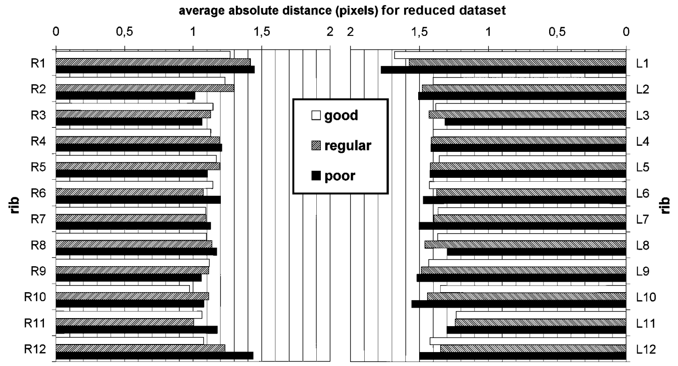

Fig. 17. Average absolute distance, in pixels, between detected rib border pixels and reference rib border pixels for good, regular and poor radiographs in the reduced subsets. When all rib levels are considered together, average absolute errors of each of these three subsets are: good: 1.221 pixels, regular: 1.254 pixels, poor: 1.259 pixels.

When all rib levels are considered together, the average absolute distances for the reduced data subsets for good, regular and poor image qualities are 1.221, 1.254 and 1.259 pixels respectively.

Analyzing these results, it can be seen that the proposed method is very well suited for detecting borders of scoliotic ribs. The overall 2D detection accuracy of 1.24 pixels (average absolute distance) outperforms most of the studies for which an average absolute distance in pixels is given in the literature. Looking at Fig. 17, the average absolute distance seems to be distributed quite uniformly among rib levels. The proposed algorithm thus seems robust under many circumstances, except perhaps for the first and twelfth rib levels, where slightly higher average absolute distances were observed. This may be partly explained by the poorer edge contrast that these first and last ribs generally present. Another important observation from Fig. 17 is that the left ribs are generally less accurately detected than the right ribs. This asymmetry in the results may be related with structural asymmetries associated with the scoliotic deformity itself. In fact, 40 of the 44 detected chest radiographs contain right thoracic or thoraco-lumbar curves. Typically, on the convex side (right side) of the spinal curve, the ribs are spread out and lie farther from each other, whereas on the concave side (left side), the ribs are closer to each other and mutual overlapping is greatly increased. Since there is obviously a link between structure overlapping and edge detection power in computer vision, this could explain why our detection results are usually better on the right patient side. The asymmetry in the results may also be explained by the presence of the heart, which generally occupies a significant area in the vicinity of the left lung. This could interfere with the detection power, as the ribs' edge contrast tends to diminish in that region. Finally, analyzing the method's robustness under various image quality levels in Fig. 17, it is notable that the detection accuracy barely decreases as image quality goes down. However, when looking at the complete dataset, large differences in average absolute distance appeared between the good, regular and poor image quality subsets. This tends to indicate that radiographic image quality does not really influence the rib detection accuracy itself, but rather increases the likelihood for the algorithm to diverge from the real rib border as image quality deteriorates. This behavior tells us that the underlying detection mechanism of the proposed method is well suited to follow rib borders even under poor contrast, but it also draws attention to the limits of our implementation of the edge-following paradigm.

When comparing our results with previous studies, one of the main advantages of the proposed method is its ability to detect both dorsal and ventral portions of the ribs, even in the presence of scoliotic deformities. In Table I, the average user interaction time with our system was 348 seconds per radiograph, *i.e.* less than 6 minutes. So, for a complete 3D reconstruction of the ribcage (from the PA-0° and PA-20° radiographs), our method is 10 times faster (strictly considering the user's workload, not CPU time) than the previous manual technique [1]. For the moment, however, the associated mean CPU time is still very long (41 minutes to process a complete radiograph), since the method has not been implemented in an optimized programming language. A C++ implementation would greatly reduce the computation time.

Robustness and repeatability of the proposed algorithm were ascertained by studying inter-technician variability, as described in section II-F above. Detection results for this additional experiment were gathered on all 1,080 processed ribs (3 users x 15 images x 24 ribs per image). The mean detection errors were -0.0017 ± 1.75 pixels, 0.00037 ± 1.76 pixels and 0.00088 ± 1.68 pixels for users 1, 2 and 3 respectively. Moreover, the overall detection ratios were 88.6%, 90.6% and 98.5% respectively. Comparing these results with the mean detection error of 0.0026 ± 1.21 pixels and rib detection ratio of 93% in Table I, we can reasonably say that the effect of inter-technician variation on detection error is low. The small increase in mean error (from 1.21 to 1.73 on average for the 3 users) can be ascribed to the fact that these users were not as well trained as the radiological technician to perform the manual selections. Meanwhile, the average detection ratio for the 3 users, 92.6%, is the same as in the original results. Therefore, our proposed method can be considered robust with respect to variability of manual inputs.

Finally, a Student t-test revealed that there were no statistical differences between the mean errors for the PA-0° and PA-20° error distributions.

IV. CONCLUSION

We have presented a novel method for semi-automatic detection of scoliotic rib borders (dorsal and ventral portions) in PA-0° and PA-20° chest radiographs. The method was tested on 44 chest radiographs of scoliotic patients. We have shown that it is possible to detect actual rib borders (instead of rib midlines) at any rib level (1 to 12) with very good accuracy, and in a shorter time than is currently needed with the manual detection method. 93% of all tested ribs were effectively detected with the proposed semi-automatic method. The overall detection error and average absolute distance were 0.0026 ± 1.21 pixels and 1.24 pixels respectively when excluding samples associated with cases where the algorithm lost track of the rib border. When considering all samples, the overall accuracy (average absolute distance) drops to 2.64 pixels, which is still better than reported results in the literature. It was shown that algorithm divergence is an important issue and accounts for most of the decrease in detection accuracy when considering the complete dataset. Besides, no statistical differences were observed between PA-0º and PA-20º results in terms of detection accuracy. Average user interaction time to process both radiographs (PA-0º and PA-20º) was slightly under 12 minutes, which is ten times less that the two hours required by the existing manual method. The CPU time for our method, however, has yet to be evaluated using a compiled implementation.

Even though the present algorithm still requires user interaction, the detection of rib borders will allow an automatic computation of the rib midlines in each view. Therefore, the 3D reconstruction of the rib midlines will not depend on the user and the accuracy of the 3D ribcage model should improve thanks to an automatic detection and matching of the rib midlines between the two views. Furthermore, the proposed method will enable the development of a new 3D reconstruction technique that could provide more personalized 3D models of the ribcage, considering that full information from rib borders would be used instead of just fitting generic rib 3D models onto reconstructed rib midlines. Finally, an accurate and personalized 3D reconstruction of the rib cage will allow clinicians to take into account the main concern of the patient, which is the rib hump that affects his/her external appearance, in the clinical assessment of scoliotic deformities.

ACKNOWLEDGMENT

The authors would like to thank Philippe Labelle, radiology technician at Sainte-Justine University Hospital Center, for having provided and manually detected all the radiographs used in this work. They would also like to acknowledge the different reviewers for their helpful comments and criticisms which have greatly improved this paper.

REFERENCES

[1] Delorme, S., Petit, Y., de Guise, J. A., Labelle, H., Aubin, C.-E., and Dansereau, J., "Assessment of the 3-D reconstruction and high-resolution geometrical modeling of the human skeletal trunk from 2-D radiographic images", *Biomedical Engineering, IEEE Transactions on*, vol. 50, no. 8, pp. 989-998, 2003.

[2] Toriwaki, J. I., Suenaga, Y., Negoro, T., and Fukumura, T., "Pattern recognition of chest X-ray images", *1st International Joint Conference on Pattern Recognition, 30 Oct.-1 Nov. 1973*, pp. 125-37, 1973.

[3] Wechsler, H. and Sklansky, J., "Finding the rib cage in chest radiographs", *Pattern Recognition*, vol. 9, no. 1, pp. 21-30, 1977.

[4] De Souza, P., "Automatic rib detection in chest radiographs", *Computer Vision, Graphics, and Image Processing*, vol. 23, no. 2, pp. 129-61, 1983.

[5] Sanada, S., Doi, K., and MacMahon, H., "Image feature analysis and computer-aided diagnosis in digital radiography: automated delineation of posterior ribs in chest images", *Medical Physics*, vol. 18, no. 5, pp. 964-71, 1991.

[6] Zhanjun Yue, Goshtasby, A., and Ackerman, L. V., "Automatic detection of rib borders in chest radiographs", *IEEE Transactions on Medical Imaging*, vol. 14, no. 3, pp. 525-36, 1995.

[7] Persoon, E., "New Edge Detection Algorithm and its Applications in Picture Processing", *Computer Graphics and Image Processing*, vol. 5, no. 4, pp. 425-446, 1976.

[8] Kulick, J. H., Challis, T. W., Brace, C., Christodoulakis, S., Merritt, I., and Neelands, P., "An image processing laboratory for automated screening of chest X-rays", *3rd International Joint Conference on Pattern Recognition, 8-11 Nov. 1976*, pp. 233-7, 1976.

[9] Shiek, C. F., Fong, C. P., Savol, A. M., Li, C. C., Sze, T. W., Preston, K. Jr., Sashin, D., and Hoy, R., "An algorithm for rib extraction in chest X-rays for pneumoconiosis detection", *The 30th Annual Conference on Engineering in Medicine and Biology, 5-9 Nov. 1977*, pp. 78, 1977.

[10] Perdriolle, R., Boffelli, N., and Ousset, M. "*La scoliose : son étude tridimensionnelle*", Paris : Maloine, 1979.

[11] Van Ginneken, B. and ter Haar Romeny, B. M., "Automatic delineation of ribs in frontal chest radiographs", *Medical Imaging 2000: Image Processing, Feb 14-Feb 17 2000*, pp. 825-836, 2000.

[12] Mouren, S., "Reconstruction 3D biplanaire de cages thoraciques scoliotiques à l'aide de modèles déformables de côtes 2003". Master's thesis, École Polytechnique de Montréal - Département de Génie Mécanique, 2003.

[13] Benameur, S. , Mignotte, M., Destrempes, F., and De Guise, J. A., "Three-dimensional biplanar reconstruction of scoliotic rib cage using the estimation of a mixture of probabilistic prior models", *IEEE Transactions on Biomedical Engineering*, vol. 52, no. 10, pp. 1713-28, 2005.

[14] Loog M., van Ginneken B., "Segmentation of the posterior ribs in chest radiographs using iterated contextual pixel classification". *IEEE Trans actions on Medical Imaging*, vol. 25, no. 5, pp. 602-611, 2006.

[15] Suzuki, K., Abe H., MacMahon H., Doi K., "Image-processing technique for suppressing ribs in chest radiographs by means of massive training artificial neural network (MTANN)", *IEEE Transactions on Medical Imaging*, vol. 25, no. 4, pp. 406-416, 2006.

[16] F. Plourde, F. Cheriet, and J. Dansereau, "Semi-automatic Detection of Scoliotic Rib Borders Using Chest Radiographs," Research into Spinal Deformities 5, IOS Press, 2006, pp. 533–537.

[17] Koehler, C, Wischgoll, T, "Knowledge-Assisted Reconstruction of the Human Rib Cage and Lungs", *IEEE Computer Graphics and Applications*, vol. 30, no. 1, pp. 17–29, 2010.

[18] Tong, R., Dong, J., and Wang, G., "Approach for contour following", *High Technology Letters*, vol. 5, no. 2, pp. 53-58, 1999.

[19] Kovacs, T., "An edge following algorithm and its application", *Periodica Polytechnica Electrical Engineering*, vol. 38, no. 2, pp. 175-90, 1994.

[20] Soille, P. "Morphological image analysis: principles and applications", Berlin: Springer, 2003.

[21] Freeman, W. T. and Adelson, E. H., "The design and use of steerable filters", *Pattern Analysis and Machine Intelligence, IEEE Transactions on*, vol. 13, no. 9, pp. 891-906, 1991.

[22] Weisstein, E. W. "*CRC concise encyclopedia of mathematics*", Boca Raton, Flor. : Chapman & Hall/CRC, 1999.

[23] Wang, J. and Howarth, P. J., "Edge following as graph searching and Hough transform algorithms for lineament detection", IGARSS'89 - Twelfth Canadian Symposium on Remote Sensing Part 1 (of 5), Jul 10-14 1989: Digest - International Geoscience and Remote Sensing Symposium (IGARSS), vol. 1, pp. 93-96, 1989.

[24] Wong, W. H. and Ip, H. H. S., "Heuristic strategy for feature matching in parallel curve detection", *1995 IEEE International Conference on Systems, Man and Cybernetics. Intelligent Systems for the 21st Century, 22-25 Oct. 1995*, pp. 4273-8, 1995.

[25] Wong, W. H. and Ip, H. H. S., "On the detection of parallel curves: models and representations", *International Journal of Pattern Recognition and Artificial Intelligence*, vol. 10, no. 7, pp. 813-27, Nov, 1996.

[26] Ip, H. H. S. and Wong, W. H., "Detecting perceptually parallel curves: criteria and force-driven optimization" *Computer Vision and Image Understanding*, vol. 68, no. 2, pp. 190-208, Nov, 1997.

[27] Kass, M., Witkin, A., and Terzopoulos, D., "Snakes: active contour models", *International Journal of Computer Vision*, vol. 1, no. 4, pp. 321-31, 1987.

[28] Lee, E. T. Y., "Choosing nodes in parametric curve interpolation", *Computer Aided Design*, vol. 21, no. 6, pp. 363-70, Jul, 1989.

[29] Wicke, L., Firbas, W., and Schmiedl, R. "*Atlas of radiologic anatomy*", Baltimore, Mar. : Urban & Schwarzenberg, 1982.